Computation of Vortical Interaction for a Sharp-Edged Double-Delta Wing

C.-H. Hsu* and P.-M. Hartwich†
Vigyan Research Associates, Inc., Hampton, Virginia
and
C. H. Liu‡
NASA Langley Research Center, Hampton, Virginia

An implicit finite-difference scheme is used to compute the three-dimensional incompressible laminar vortical flow around a sharp-edged double-delta wing with an aspect ratio of 2.06. By adding a time derivative of the pressure to the continuity equation, the unsteady incompressible Navier-Stokes equations can be integrated like a conventional parabolic time-dependent system of equations. The flux-difference split scheme combines approximate factorization in crossflow planes with a symmetric planar Gauss-Seidel relaxation in the remaining spatial direction. Up to second-order spatial accuracy is achieved by using an upwind differencing similar to a total variation diminishing scheme. Computations are performed at $Re = 1.4 \times 10^6$ and $\alpha = 20$ deg. Numerical results indicate that the first-order-accurate scheme is unable to capture the wing vortex, while the second-order-accurate scheme has successfully simulated the vortical interaction between the strake and wing vortices.

Introduction

TO obtain valuable visual information, diagnostic water tunnels, towing tanks, and low-speed wind tunnels have been extensively used in aerodynamic design and reshaping. Organized vortical flows are successfully employed in generating and controlling useful nonlinear lift for many modern aircraft. These vortices are usually associated with slender delta-like wings and/or strake-wing configurations. Wings with kinked leading edges such as double-delta wings or strake wings are often designed to obtain a favorable interaction between the strake leading-edge vortex and the main-wing flow. The strong and stable vortices originating from the highly swept strake can delay large-scale boundary-layer flow separation on the upper surface of the main wing or stabilize the leading-edge vortices emanating from the main wing. Low-speed wind-tunnel investigations[1,2] on double-delta wings indicate that at low angles of attack (α) two primary vortices are shed leeward on each side of the wing, originating from the strake and wing leading edges, and remain distinguishable over the entire wing. At medium angles of attack, they wrap around each other and merge into one stable vortex over the rear part of the wing. At high angles of attack, they merge right after the kink and are no longer separate. At very high angles of attack, the large-scale vortex breakdown occurs over the wing and the induced vortical lift diminishes. Numerical simulations for those low-speed phenomena have motivated the current development of a fast and reliable computational method for three-dimensional incompressible flow.

Various three-dimensional Navier-Stokes codes have been mainly developed for compressible flow. Applying these codes to simulations of incompressible flow is not efficient and is generally not recommended. There are two methods using primitive variables for solving incompressible flows. The method of solving Poisson's equation for pressure was developed by Harlow and Welch.[3] This procedure normally requires a relaxation scheme iterating on pressure at each time step until the divergence-free condition is satisfied. On the other hand, Chorin[4] proposed to use artificial compressibility in solving the continuity equation. By adding a time derivative of the pressure to the continuity equation, the unsteady incompressible Navier-Stokes equations can be integrated like a conventional parabolic time-dependent system of equations. This results in a system of equations that can be efficiently solved with an implicit scheme.[5-9]

Most of the flowfield is dominated by convection for high-Reynolds number flows. Furthermore, the Navier-Stokes equations reduce to hyperbolic Euler equations as the Reynolds number approaches infinity. This suggests that the ideas for solving the Euler equations can be extended to the Navier-Stokes equations. Upwind schemes for solving the Euler equations have gained considerable popularity. Upwind differencing alleviates the necessity to add and tune the numerical dissipation for numerical stability and accuracy as in the schemes with central differencing.[5,6] In addition, one-sided differencing makes the coefficient matrices diagonally dominant. These features lead to the development of several upwind schemes[7-9] for solving the unsteady incompressible Navier-Stokes equations.

The purpose of this study is to apply one of the new implicit upwind schemes[8,9] to compute the flow about a sharp-edged double-delta wing with an aspect ratio of 2.06 and a maximum thickness of 0.03. This configuration (Fig. 1) has a leading-edge kink at midchord and has 76- and 60-deg sweep for the leading edges of the strake and main wing, respectively. Cross sections are triangular ahead of and trapezoidal behind the 40% chord station. The upper surface of the wing is flat, and all leading edges and the trailing edge are chamfered on the windward side of the wing (about 17-deg angle normal to the edge). This geometry was tested in a low-speed wind tunnel[2] at $Re = 1.4 \times 10^6$ and $M_\infty \approx 0.1$. A laser-sheet visualization technique was employed to investigate the streamwise development of vortical flow above the double-delta wing at an angle of attack of 20 deg. Above the strake the flow is similar to the flow above the forward half of a slender delta wing. The flow is dominated by two near-coni-

Presented as Paper 87-0206 at the AIAA 25th Aerospace Sciences Meeting, Reno, NV, Jan. 12-15, 1987; received Jan. 21, 1987; revision received Oct. 2, 1987.

*Research Scientist. Senior Member AIAA.
†Research Scientist. Member AIAA.
‡Senior Research Scientist. Senior Member AIAA.

cal leading-edge vortices. The shear layers that emanate from the strake leading edges roll up into the so-called strake vortices. Downstream of the leading-edge kink an additional vortex, the wing vortex, is formed above each side of the main wing. Since these two vortices have the same sense of rotation, they swirl around each other due to mutual induction. The wing vortex is a double-branched vortex because one shear layer is connected to the wing leading edge and the other one to the strake vortex. The wing vortex is continuously fed with vorticity from the wing leading edge as well as from the shear layer between wing and strake vortices. As a consequence, the vortical strength of wing vortex increases downstream. At some distance downstream of the kink the vorticity fed into the strake vortex will gradually diminish. Consequently, the vortical strength of the strake vortex will become constant or even reduce because vorticity is swallowed by the stronger wing vortex. Downstream of the 85% chord station, the two vortices completely merge into one single vortex.

In the next section, the governing equations are presented. Then a brief outline of the numerical method is followed. Thereafter, computed results are presented and compared with experimental data.

Governing Equations

By adding p_t/β to the continuity equation, the time-dependent, three-dimensional, incompressible Navier-Stokes equations in conservation-law form for a body-fitted coordinate system are formulated as follows:

$$[Q/J]_t + [E - E_V]_\zeta + [F - F_V]_\xi + [G - G_V]_\eta = 0 \tag{1}$$

with

$$\begin{bmatrix} E - E_V \\ F - F_V \\ G - G_V \end{bmatrix} = \begin{bmatrix} \zeta_x/J & \zeta_y/J & \zeta_z/J \\ \xi_x/J & \xi_y/J & \xi_z/J \\ \eta_x/J & \eta_y/J & \eta_z/J \end{bmatrix} \begin{bmatrix} [E - E_V]_C \\ [F - F_V]_C \\ [F - G_V]_C \end{bmatrix}$$

where

$$Q = [p, u, v, w]^T$$

$$E_C = [\beta u, u^2 + p, uv, uw]^T$$

$$F_C = [\beta v, uv, v^2 + p, vw]^T$$

$$G_C = [\beta w, uw, vw, w^2 + p]^T$$

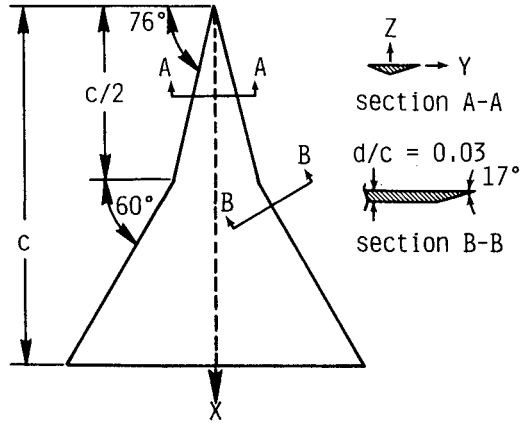

Fig. 1 Sharp-edged double-delta wing with an aspect ratio of 2.06.

and

$$E_{V,C} = Re^{-1}[0, 2u_x, u_y + v_x, u_z + w_x]^T$$

$$F_{V,C} = Re^{-1}[0, v_x + u_y, 2v_y, v_z + w_y]^T$$

$$G_{V,C} = Re^{-1}[0, w_x + u_z, w_y + v_z, 2w_z]^T$$

Assuming a time-invariant grid, the Jacobian of the coordinate transformation J is defined as

$$J = \det[\partial(\zeta, \xi, \eta)/\partial(x, y, z)] \tag{2}$$

The preceding equations are written in dimensionless form. The Cartesian coordinates x, y, and z are nondimensionalized with the root-chord length c of the wing. The Cartesian velocities u, v, and w are normalized with the freestream velocity V_∞. The time t is nondimensionalized with c/V_∞, and the normalized pressure is defined as $p = (P - P_\infty)/\rho_\infty V_\infty^2$. The density does not require any normalization since it is simply a constant. For a constant viscosity μ, the Reynolds number is defined as $Re = \rho_\infty V_\infty c/\mu$.

The artificial time derivative of the pressure couples the continuity equation with the momentum equations. The parameter β is a measure for the amount of artificial compressibility. For very large β, the modified governing equations resemble the Navier-Stokes equations for truly incompressible flow. However, as $\beta \to \infty$, the governing equations become very stiff. On the other hand, if β is chosen to be too small, the upstream influence of a local pressure disturbance is nearly lost, i.e., the system of equations becomes subsonically incompatible. For steady-state calculations, β is set to unity as in Refs. 7–12. When a steady state is approached ($p_t \to 0$), the effect of the pseudocompressibility diminishes, resulting in an incompressible solution.

Numerical Algorithm

Control-Volume Approach

Each grid point is defined as the centroid of a control volume. Its six bounding surfaces are located at the six nearest half-grid points. The dependent variables are specified at each centroid and the numerical fluxes are formulated at its six bounding surfaces. At control-volume interfaces, u, v, w, p, and the differences of u, v, and w occurring in the cross-derivative terms of the viscous fluxes and the metric quantities are obtained by taking simple arithmetic averages of their values at neighboring full-grid points.

To maintain a source-free differencing, the metrics are differenced using a weighted-average procedure.[8,13] For example,

$$(\zeta_x)_{ijk} = J_{ijk}[(\sigma_k\delta_j y)(\sigma_j\delta_k z) - (\sigma_j\delta_k y)(\sigma_k\delta_j z)]_i \tag{3}$$

with

$$\sigma_k\delta_j y = [(\delta_j y)_{k+1} + (\delta_j y)_{k-1}]/2$$

and δ is the usual central-difference operator. This special averaging procedure brings the present finite-difference method close to a finite-volume approach.

Flux-Difference Splitting

Since upwind differencing simulates the wave propagation properties of hyperbolic equations and because it does not need artificial viscosity terms, it is applied to the inviscid fluxes E, F, and G. For incompressible flow, these inviscid fluxes are not homogeneous of degree one in the state vector Q. Hence, the usual flux-vector splitting methods[14,15] do not work here. A flux-difference splitting based on Roe's approximate Riemann solver[16] is chosen to upwind-difference the inviscid fluxes. To incorporate the idea of flux-difference

splitting, the three-dimensional conservation laws are first dimensionally split into three one-dimensional systems of equations through the operator-split concept:

$$[Q/J]_t + H_\theta = 0 \tag{4}$$

where $\theta = \zeta$, ξ, or η and $H = E$, F, or G. The essential idea in Roe's scheme is to find approximate solutions to Eq. (4) by constructing exact solutions to an approximate problem, i.e.,

$$[Q/J]_t + D_l \Delta_l Q = 0 \tag{5}$$

where $\Delta_l(\ ) = [(\ )_{l+1/2} - (\ )_{l-1/2}]/\Delta\theta$ and $l = i$, j, or k. The locally frozen matrix D of the preceding semidiscrete formulation has the same eigenvalues as $\partial H/\partial Q$, if $D(Q_l, Q_{l+1}) \to (\partial H/\partial Q)(Q_l, Q_{l+1})$ for $Q_{l+1} \to Q_l$. Furthermore, Eq. (5) is conservative if $D(Q_l, Q_{l-1}) \times (Q_l - Q_{l-1}) = H_l - H_{l-1}$. For compressible flow,[16] the mean coefficient matrix D must be evaluated using Roe's specially averaged values of the elements of Q. For incompressible flow,[7-12] the special averaging reduces to an arithmetic average, e.g., $D_{l+1/2} = D(Q_{l+1/2}) = D[(Q_l + Q_{l+1})/2]$. In the latter subsections, $D = A$, B, or C in the ζ, ξ, or η directions, respectively.

The eigenvalues λ_m ($m = 1,2,3,4$) of D represent the wave speeds of the Riemann problem. By using a similarity transformation, D can be split as

$$D = R\Lambda L = R[\Lambda^+ - \Lambda^-]L = D^+ - D^- \tag{6}$$

where R and L are right and left eigenvectors of D with $LR = I$ (I is the identity matrix). The diagonal matrix Λ consists of λ_m as its elements and $\Lambda^\pm = [|\Lambda| \pm \Lambda]/2$. The detailed formulae for the eigenvalues and eigenvectors can be found in Refs. 8 and 9. Introducing Eq. (6), a first-order semidiscrete formulation of Eq. (5) is given by

$$[Q/J]_t + D^+_{l-1/2}\Delta_{l-1/2}Q^n - D^-_{l+1/2}\Delta_{l+1/2}Q^n = 0 \tag{7}$$

Applying first-order, Euler backward-time differencing, Eq. (7) is rewritten as

$$\left[I/J\Delta t + D^+_{l-1/2}\Delta_{l-1/2} - D^-_{l+1/2}\Delta_{l+1/2}\right]^n \Delta Q^n = \left[D^-_{l+1/2}\Delta_{l+1/2} - D^+_{l-1/2}\Delta_{l-1/2}\right]^n Q^n \tag{8}$$

where

$$\Delta Q^n = Q^{n+1} - Q^n$$

Equation (8) describes the influence of a right-traveling wave from the left and a left-traveling wave from the right on Q at the centroid l. This simple flux-difference splitting based on Roe's approximate Riemann solver is used separately in each spatial dimension. For three-dimensional conservation laws, the overall discretization is obtained via adding up all three independent discretizations of the flux vectors in each dimension.

High-Resolution TVD Scheme

Equation (8) gives first-order-accurate spatial differencing. Its solution is contaminated with a considerable amount of numerical dissipation. The spatial differencing is enhanced to second-order accuracy by incorporating a discretization similar to a total variation diminishing (TVD) scheme. TVD schemes are essentially nonlinear schemes. They switch between several difference stencils such that the schemes adapt to the local solution in order to give high resolution in regions of smooth solution while still suppressing spurious oscillations in regions of rapid changes in gradient (e.g., contact discontinuities). Here, the high-resolution scheme is based on a recently developed implicit TVD scheme for linear systems of one-dimensional hyperbolic conservation laws. For a linear system of equations, the quantities whose total variation can be forced to diminish in time are the characteristic variables[17,18] defined as

$$W = LQ \tag{9}$$

Substituting Eq. (9) into Eq. (8) gives

$$\left[(1/\Delta tJ) + \lambda^+_m\Delta_{l-1/2} - \lambda^-_m\Delta_{l+1/2}\right]^n \Delta W^n_m = \left(\lambda^-_m\Delta_{l+1/2} - \lambda^+_m\Delta_{l-1/2}\right)^n W^n_m \tag{10}$$

Equation (10) describes four decoupled, scalar linear hyperbolic conservation laws and is unconditionally TVD. The extension to a second-order TVD scheme is achieved by rewriting Eq. (10) as follows:[9]

$$\left[(1/\Delta tJ) + \lambda^+_m\Delta_{l-1/2} - \lambda^-_m\Delta_{l+1/2}\right]^n \Delta W^n_m = \left\{\lambda^-_m\left[1 - 0.5\left(\phi^-_{m,l+1} - \phi^+_{m,l}\right)\right]\right\}^n \Delta_{l+1/2}W^n_m - \left\{\lambda^+_m\left[1 + 0.5\left(\phi^-_{m,l} - \phi^+_{m,l-1}\right)\right]\right\}^n \Delta_{l-1/2}W^n_m \tag{11}$$

where

$$\phi^\pm_{m,l} = \max\left[0; 2 \times \min\left(r^\mp_{m,l\pm1}; 1\right)\right] \tag{12}$$

$$r^\pm_{m,l} = \left(\Delta_{l-1/2}W^n_m/\Delta_{l+1/2}W^n_m\right)^{\pm1} \text{ for } \Delta_{l\pm1/2}W^n_m \neq 0$$

or

$$r^\pm_{m,l} = 0 \text{ for } \Delta_{l\pm1/2}W^n_m = 0$$

Equation (11) with Eq. (12) comprises several difference approximations. The stencil depends on the local TVD limiter $\phi^\pm_{m,l}$. When all ϕ_m equal zero, Eq. (11) gives first-order upwind differencing. For any other combination of ϕ_m, it resembles central, one-sided or upwind biased differencing of second-order accuracy. The extension of Eq. (11) to a nonlinear system of conservation laws is obtained in two steps. First, the nonlinear equivalent for Eq. (11) is formed. Then it is multiplied by R from left to get[9]

$$\left(I/\Delta tJ + D^+_{l-1/2}\Delta_{l-1/2} - D^-_{l+1/2}\Delta_{l+1/2}\right)^n \Delta Q^n = \left\{R_{l+1/2}\Lambda^-_{l+1/2}\left[I - 0.5\left(\Phi^-_{l+1} - \Phi^+_l\right)\right]L_{l+1/2}\right\}^n \Delta_{l+1/2}Q^n - \left\{R_{l-1/2}\Lambda^+_{l-1/2}\left[I + 0.5\left(\Phi^-_l - \Phi^+_{l-1}\right)\right]L_{l-1/2}\right\}^n \Delta_{l-1/2}Q^n \tag{13}$$

where

$$\Phi^\pm_l = \text{diag}\left(\phi^\pm_1, \phi^\pm_2, \phi^\pm_3, \phi^\pm_4\right)_l$$

Factorization and Relaxation

The solutions to Eq. (1) are advanced in pseudotime using Euler-implicit time differencing and local time stepping. An implicit scheme is chosen to avoid a restrictive time-step size when highly refined grids are used to resolve viscous effects. Casting the equations in delta form yields steady-state solutions that are independent of the time-step size. The two-time-level discretization of Eq. (1) can be written as

$$N\Delta Q^n + RES(Q^n) = 0 \tag{14}$$

The operator RES gives the residual at time level n and represents the discretized spatial-derivative terms of Eq. (1). The viscous fluxes are centrally differenced in the usual manner,[13] and the inviscid fluxes are discretized by applying the general formulation in Eq. (13). The resulting spatial differencing is up to second-order-accurate. A hybrid approach[8,9] for the formulation of the operator N is chosen. It uses approximate factorization in crossflow planes (ξ-η planes) in combination with a symmetric planar Gauss-Seidel relaxation in the ζ direction. The hybrid scheme with block-tridiagonal implicit factors is written as

$$\left[M+(B^{+}+S^{*})_{j-1/2}\Delta_{j-1/2}-(B^{-}+S^{*})_{j+1/2}\Delta_{j+1/2}\right]^{n}\times(M^{-1})^{n}\left[M+(C^{+}+T^{*})_{k-1/2}\Delta_{k-1/2}-(C^{-}+T^{*})_{k+1/2}\Delta_{k+1/2}\right]^{n}\Delta Q^{n}=-RES(Q^{n},Q^{n+1}) \tag{15}$$

with

$$M=I/\Delta tJ+(A^{+}+R^{*})_{i-1/2}+(A^{-}+R^{*})_{i+1/2}$$

where R^{*}, S^{*}, and T^{*} are the linearized coefficient matrices associated with viscous shear fluxes E_V, F_V, and G_V, respectively.[8,13] The nonlinear updating of the residual during back and forth sweeps in the ζ direction is indicated by $RES(Q^{n},Q^{n+1})$ in Eq. (15).

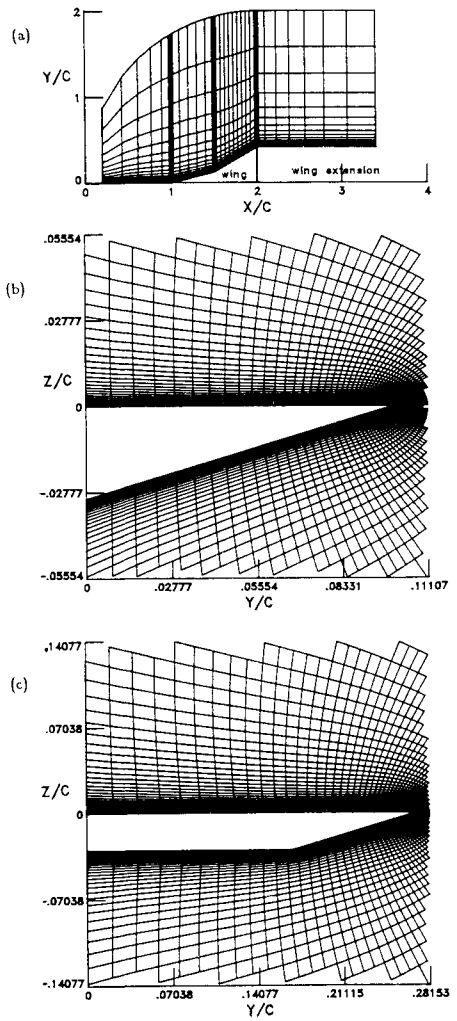

Fig. 2 Three-dimensional elliptic grid: a) planform view, b) crossplane grid at 40% c, and c) crossplane grid at 75% c.

Boundary and Initial Conditions

Unknown values of Q^{n} on the boundaries are updated explicitly and ΔQ^{n} is set to zero. On the wing surface, the no-slip condition is imposed and the normal gradient of the pressure is assumed to vanish. Freestream conditions are specified along the outer boundaries except for the outflow boundary, where the values are computed from extrapolation. Reflection conditions are applied on the symmetry plane. The flowfield values along the branch cut in the wake are computed by averaging the extrapolates of the dependent variables from above and below. The initial conditions consist of freestream values. The values of $\phi^{\pm}_{m,l}$ along all boundaries are set to zero.

Computed Results

A grid of 531,069 points is generated plane by plane by solving a set of elliptic partial differential equations.[19] The shape of the computational domain is described by a frustum of half-hemispherical cylinder with a radius of $2c$. As shown in Fig. 2a, the grid extends $0.8c$ upstream of the apex ($x/c=1.0$) and $1.4c$ downstream of the trailing edge ($x/c=2.0$). The C-H grid is segmented into 77 crossflow planes perpendicular to the longitudinal axis of the wing. In each crossplane (Figs. 2b and 2c), there are 57 and 121 grid points in the radial and circumferential directions, respectively. The maximum spacing normal to the wing surface for the first grid

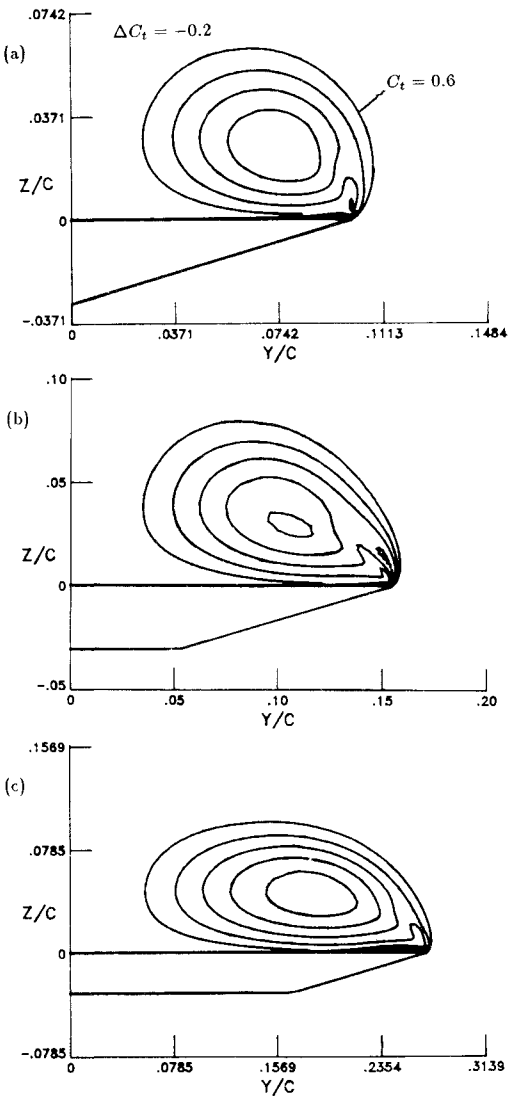

Fig. 3 Total pressure contours with first-order accuracy at a) 40% c, b) 55% c, and c) 75% c.

line encircling the wing at the trailing edge is $2.5 \times 10^{-4}c$. Cross sections are clustered near the apex, kink, and trailing edge. The minimum spacing between crossplanes is $6.25 \times 10^{-3}c$.

The finite-difference solutions at $Re = 1.4 \times 10^6$ and $\alpha = 20$ deg are carried out in 32-bit word arithmetic on the CDC CYBER 205 vector computer at NASA Ames Research Center. The central processor unit time per grid point per iteration is 37.3 μs. The L_2 norm of all residuals is reduced by three orders of magnitude within about 500 (1000) iterations for first-order- (second-order-) accurate computations. This is achieved with local time stepping ($CFL = 10$).

Computed total pressure contours at 40, 55, and 75% chord stations are shown in Figs. 3 and 4 for first- and second-order-accurate results, respectively; C_t is the total pressure coefficient, and its value at the farfield is 1. Both figures show that the total pressure loss occurs mainly along the wing surface, the leading-edge separated shear layers, and the vortical cores. Figure 3 displays computed total pressure contours with first-order accuracy. The flow rolls up into a strong primary strake vortex (Fig. 3a), and this vortex induces a tiny secondary vortex. Figures 3b and 3c indicate that the sizes of the primary and secondary vortices become larger as the flow approaches the trailing edge. The global vortical flowfield[10] is qualitatively similar to the experimental observations.[2] However, the primary wing vortex is too weak to show up or merges with the primary strake vortex right at the kink station. This implies that the first-order one-sided differences for the inviscid fluxes have introduced too much numerical damping and have smeared out the shedding of the wing vortex.

Figure 4 shows computed total pressure contours with second-order accuracy. Upstream of the kink, at 40% c, only the primary strake vortex exists (Fig. 4a). Since the vorticity is stronger due to better flow resolution, the size of vortex is smaller and the total pressure loss is larger than those corresponding values with first-order accuracy at the same chord stations. The secondary separation induced by the adverse pressure gradient due to the primary strake vortex is much clearer than that with first-order accuracy. Downstream of the kink, at 55% c, an additional vortex of the same sense of rotation, the primary wing vortex, is clearly indicated in Fig. 4b. Further downstream, the weaker strake vortex moves downward and outboard and the stronger wing vortex drifts slightly upward and inboard. At 75% c (Fig. 4c), the two primary vortices almost merge into one single vortex and induce a large secondary vortex. Lateral trajectories (locations of local total pressure minima) of the interacting primary vortices are plotted in Fig. 5. Numerical calculations are in good agreement with experimental data except that the predicted location (75% c) of complete merging is upstream of the experimental value (85% c). This discrepancy is probably caused by the laminar/turbulent transition observed in the experiment but is not modeled in the present computations. It might also be attributable to the insufficient crossflow resolution near the trailing edge.

The corresponding distributions of spanwise surface pressure coefficient are shown in Fig. 6, where s is the local half-span. The solid and dotted lines represent the second- and first-order-accurate results, respectively. Figure 6 indicates that differences between first- and second-order-accurate pressure distributions are insignificant on the lower surface of the wing. However, on the upper surface only the second-order-accurate results correctly reflect the process of vortical interaction. In addition, all suction pressure peaks with sec-

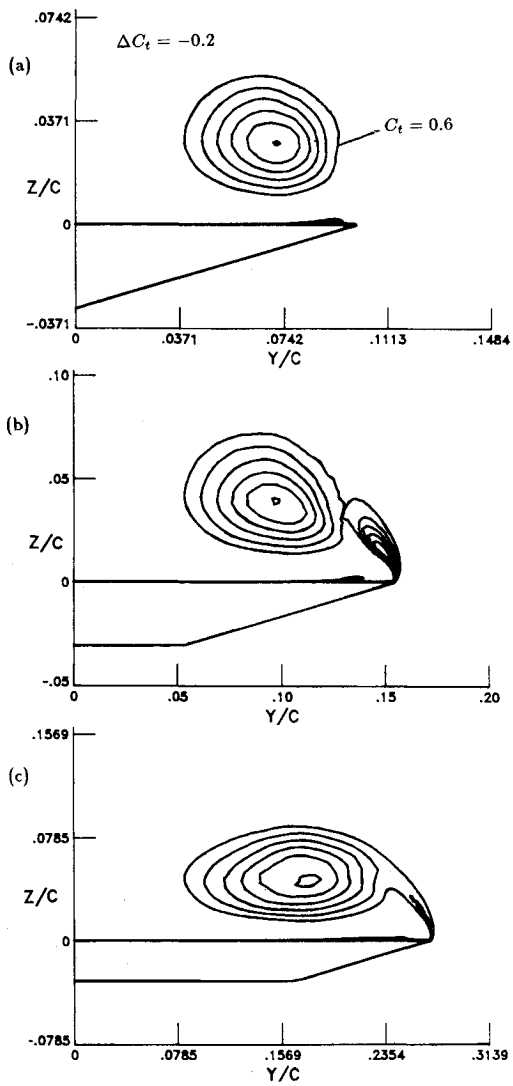

Fig. 4 Total pressure contours with second-order accuracy at a) 40% c, b) 55% c, and c) 75% c.

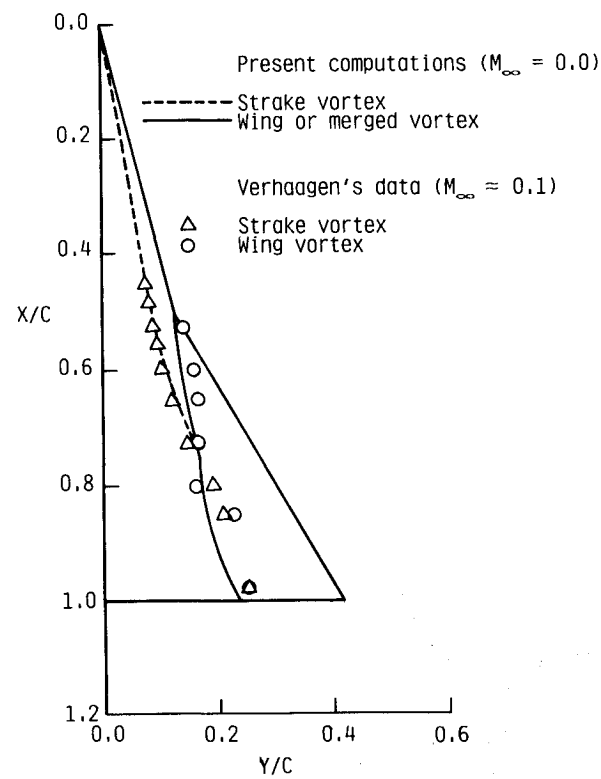

Fig. 5 Lateral trajectories of vortical cores.

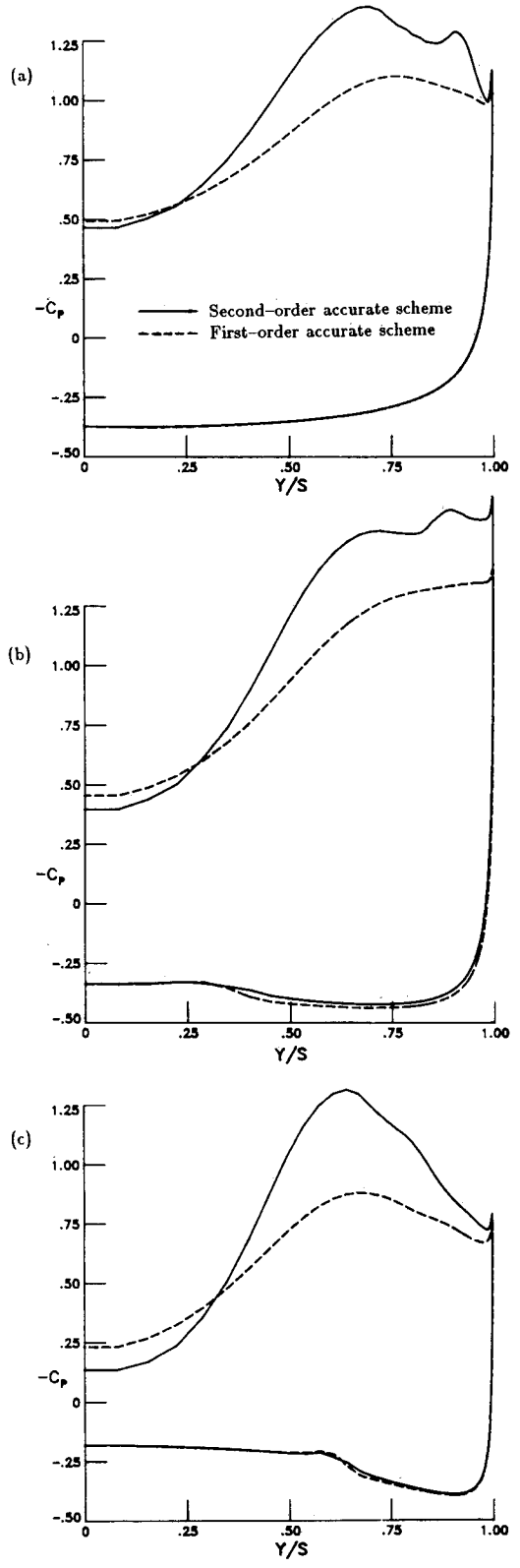

Fig. 6 Spanwise surface pressure distributions at a) 40%c, b) 55%c, and c) 75%c.

ond-order accuracy are much higher than those with first-order accuracy. Unfortunately, there are no experimental data available for comparison.

Conclusions

Navier-Stokes computations are obtained for a sharp-edged double-delta wing at $Re = 1.4 \times 10^6$ and $\alpha = 20$ deg. The first-order-accurate results indicate that the wing vortex is too weak to appear because of hefty numerical dissipation. By contrast, the second-order-accurate results reveal that both the single-branched strake vortex and the double-branched wing vortex are well captured. Furthermore, the computed lateral trajectories of vortical cores are predicted in good agreement with experimental data. It is clearly demonstrated that at least a second-order-accurate scheme is needed to simulate the vortical interaction for a double-delta wing. Further computational efforts with greater mesh resolution must be made to resolve fully the detailed structure of vortical flow. In addition, detailed experimental investigations must be carried out to provide the pressure and velocity distributions so that more quantitative comparisons between numerical results and experimental data can be performed.

Acknowledgment

This work of the first author was supported by NASA Langley Research Center under Grant NAG-1-455. The work of the second author was sponsored by NASA Langley Research Center under Contract NAS 1-17919.

References

[1]Brennenstuhl, U. and Hummel, D., "Vortex Formation over Double-Delta Wings," ICAS-82-6.6.3, Aug. 1982.

[2]Verhaagen, N.G., "An Experimental Investigation of the Vortex Flow over Delta and Double Delta Wings at Low Speed," AGARD-CP-342, Paper 7, April 1983.

[3]Harlow, F.H. and Welch, J.E., "Numerical Calculation of Time-Dependent Viscous Incompressible Flow with Free Surface," *Physics of Fluids*, Vol. 8, Dec. 1965, pp. 2182–2189.

[4]Chorin, A.J., "A Numerical Method for Solving Incompressible Viscous Flow Problems," *Journal of Computational Physics*, Vol. 2, 1967, pp. 12–26.

[5]Steger, J.L. and Kutler, P., "Implicit Finite-Difference Procedures for the Computation of Vortex Wakes," *AIAA Journal*, Vol. 15, April 1977, pp. 581–590.

[6]Kwak, D., Chang, J.L.C., Shanks, S.P., and Chakravarthy, S.R., "An Incompressible Navier-Stokes Flow Solver in Three-Dimensional Curvilinear Coordinate Systems Using Primitive Variables," AIAA Paper 84-0253, Jan. 1984.

[7]Hartwich, P.-M., Hsu, C.-H., and Liu, C.H., "Implicit, Hybrid Schemes for the Flux-Difference Splitted, Three-Dimensional Navier-Stokes Equations," *Lecture Notes in Physics*, Vol. 264, Springer Verlag, New York, 1986, pp. 303–307.

[8]Hartwich, P.-M. and Hsu, C.-H., "High Resolution Upwind Schemes for the Three-Dimensional Incompressible Navier-Stokes Equations," AIAA Paper 87-0547, Jan. 1987.

[9]Hartwich, P.-M., Hsu, C.-H., and Liu, C.H., "Vectorizable Implicit Algorithms for the Flux-Difference Split, Three-Dimensional Navier-Stokes Equations," *Journal of Fluids Engineering*, Vol. 47, June 1987, pp. 9–18.

[10]Hsu, C.-H., Hartwich, P.-M., and Liu, C.H., "Incompressible Navier-Stokes Solutions for a Sharp-Edged Double-Delta Wing," AIAA Paper 87-0206, Jan. 1987.

[11]Hsu, C.-H., Hartwich, P.-M., and Liu, C.H., "Incompressible Navier-Stokes Computations of Vortical Flows over Double-Delta Wings," AIAA Paper 87-1341, June 1987.

[12]Hsu, C.-H., Hartwich, P.-M., and Liu, C.H., "Three-Dimensional Incompressible Navier-Stokes Simulations of Slender Wing Vortices," AIAA Paper 87-2476-CP, Aug. 1987.

[13]Pulliam, T.H. and Steger, J.L., "On Implicit Finite-Difference Simulations of Three-Dimensional Flow," AIAA Paper 78-10, Jan. 1978.

[14]Steger, J.L. and Warming, R.F., "Flux Vector Splitting of the Inviscid Gasdynamics Equations with Application to Finite-Difference Methods," *Journal of Computational Physics*, Vol. 40, 1981, pp. 263–293.

[15]Van Leer, B., "Flux Vector Splitting for the Euler Equations," ICASE Rept. 82-30, Sept. 1982.

[16]Roe, P.L., "Approximate Riemann Solvers, Parameter Vectors, and Difference Schemes," *Journal of Computational Physics*, Vol. 43, 1981, pp. 357–372.

[17]Yee, H.C., Warming, R.F., and Harten, A., "Implicit Total Variation Diminishing (TVD) Schemes for Steady-State Calculations," *Journal of Computational Physics*, Vol. 57, 1985, pp. 327–360.

[18]Harten, A., "High Resolution Schemes for Hyperbolic Conservation Laws," *Journal of Computational Physics*, Vol. 49, 1983, pp. 357–393.

[19]Hartwich, P.-M., "Three-Dimensional Grids as Solutions of Elliptic Systems," AIAA Paper 86-0430, Jan. 1986.